Int J Adv Manuf Technol (2017) 92:481–495
DOI 10.1007/s00170-017-0121-8

ORIGINAL ARTICLE

An analytical investigation on the wrinkling of aluminium alloys during stamping using macro-scale structural tooling surfaces

Kailun Zheng[1] · **Junyi Lee**[1] · **Denis J. Politis**[1] · **Nan Li**[1] · **Jianguo Lin**[1] · **Trevor A. Dean**[2]

Received: 28 November 2016 / Accepted: 1 February 2017 / Published online: 27 February 2017
© The Author(s) 2017. This article is published with open access at Springerlink.com

Abstract Structural surface texturing is believed to be a promising approach to modify tribological and thermal performances of tooling for sheet-stamping processes. However, a fundamental study on the surface-texturing design and resulting material deformation is currently lacking. In this paper, an advanced analytical buckling model specifically for the utilisation of textured tools at macro-scale, comprising dislocation-driven material model, isotropic yield criteria, bifurcation theory and Donnell-Mushtari-Vlasov (DMV) shell structure theory, was established. The developed analytical buckling model was validated by cylindrical deep-drawing experiments. Further finite element (FE) simulations with the implementation of material model via user-defined subroutine were also used to validate the bucking model for large surface texture designs. Effects of theoretical assumptions, such as yield criterion, boundary condition and test-piece geometry, on the accuracy of model prediction for wrinkling were investigated. It was found that the von Mises yield criterion and hinged boundary condition exhibited more accurate predictions. In addition, the DMV shell theory made this model most representative for large structural texturing designs. Furthermore, the implementation of induced shear strain component has an important effect on precisely predicting the wrinkling occurrence. The advanced analytical models developed in this study combine various classical mechanics, structure stability and material modelling together, which provides a useful tool for tooling engineers to analyse structural designs.

Keywords Buckling model · Macro-textured tool · Aluminium alloys · Deep drawing · FE model · Flange wrinkling

1 Introduction

Tooling surface performances, such as triblogical and thermal, are believed to play an imporant role in controlling material deformation and post-strengthening for hot-stamping sheet metals [1]. In recent years, hot stamping of high-strength aluminium alloys has become a popular and promising lightweight strategy for automotive original equipment manufacturers (OEMs) due to the enviromental and fuel economy concerns [2, 3]. Considering the highly reactive and formability behaviour of high-strength aluminium alloys at elevated temperatures, tooling requirments have become more stringent [4, 5]. Tooling technologies with low interfacial friction coefficient, good wear resistance and thermal properties are urgently required. Structual surface texturing has been extensively investigated and applied in particular engineering areas due to its abilities of modifying tribological and thermal performances [6]. Surface texture can be roughly divided into micro- and macro-scales according to the texture dimension. Micro-scale surface texture, normally at micrometre or nanometre scale, is believed to be able to improve tribological properties of tool surfaces with the combination of lubricants [6]. Costa and Hutchings [7] investigated micro-scale patterned tool surface tribological performance using a strip-drawing process; a significant reduction of friction coefficient was obtained as these surface textures were believed to exhibit a reservior function for lubricant to improve the lubrication effect. In addition, wear

✉ Denis J. Politis
denis.politis06@imperial.ac.uk

[1] Department of Mechanical Engineering, Imperial College London, Exhibition Road, London SW7 2AZ, UK

[2] School of Mechanical Engineering, University of Birmingham, Edgbaston, Birmingham B15 2TT, UK

resistance of tool surfaces can also be increased as test-piece material debris during interface sliding are stored in the texture hollows. The great loss of hard particles at the tool/blank interface results in a significant improvement in wear resistance of tooling. Compared with the extensive research on micro-texturing of tool surfaces, limited research has been performed for macro-scale surface texturing. Franzen et al. [8] investigated the tribological performance of macroscopic textured tool surfaces using strip-drawing process. The textured macro-scale tool surfaces can increase the interficial friction coefficient compared to flat tool surfaces, which might be a potentional approach to replace conventional draw beads for sheet stamping.

To this extent, most research focused on fundamental triblogy studies of textured tool surfaces. However, effects of surface texturing on draw-ability and thermal properties of hot-stamping aluminium alloys have not been thoroughly studied. Zheng et al. [9] investigated the hot draw ability of aluminium alloys with a one-dimensional macro-scale textured tool surface both experimentally and numerically. A significant improvement of draw ability was achieved due to a more uniform temperature field within the blank. The reasons are that the utilisation of tool surface texture can reduce contact area between blank and tool material significantly. Moreover, the interfacial heat transfer coefficient at the texture hollow was also decreased due to the vacant space [10]. However, the texture effect was only examined for blanks under a one-dimensional stress state. For hot-stamping, complex-shaped sheet components with a two-dimensional contrary sign stress state, the compressive stress may cause material located above the texture hollow to buckle due to the absence of blankholding force constraint [11], as shown in Fig. 1 [12]. The modelling of flange-wrinkling phenomena in deep-drawing processes has been reviewed in detail by Kadkhodayan et al. [13]. To predict the induced buckling phenomena experienced when using macro-scale textured tools, Zheng et al. [12] established analytical buckling models based on Senior's beam [14] and Yu's plate structure buckling assumptions [15] for cylindrical deep-drawing tests. However, the assumption of reduced Young's modulus which is used to reflect inelastic buckling is believed to be inaccurate [13]. In addition, the beam and plate assumptions may not be suitable for tool texture designs with larger dimensions.

To address the above disadvantages, the work in this paper aims to establish an advanced buckling model based on classical elastic-plastic mechanics of solids and further extended to large surface textured tool designs. The use of constitutive relationship of an elastic-plastic solid can improve the calculation accuracy to cover the deformation behaviour at the plastic range. In this study, a more advanced analytical buckling model specifically for the metal-forming processes using macro-textured tool design was developed based on elastic-plastic solid mechanics, bifurcation theory [16] and Donnell-Mushtari-Vlasov (DMV) shell structure theory [17]. The accuracy of the developed buckling model was validated by experimentation and finite element (FE) simulations implemented with a dislocation-driven material model. Effects of related analytical assumptions and solutions, such as yield criteria and boundary condition, are discussed in detail. In addition, application ranges of the developed buckling model were also investigated. The model can provide a prediction tool for stamping tool designers. The combination of a series of classic and robust theories provides a feasible approach to modelling actual forming processes and can be a foundation for establishing buckling models of metal-forming processes in hot forming conditions in the future.

2 Analytical buckling model

2.1 Macro-textured tool design concept and modelling

Forming dies of sheet-stamping processes are normally composed of the punch, die and blankholder. Figure 2a shows the schematic diagram of a tool set with textured tool surfaces. According to the contact condition between textured tools and sheet blank, textures can be divided into a groove (texture hollow) and surface (texture top). Correspondingly, the blank material in contact with the surface was defined as zone S, whilst material located on the texture hollow (groove) was defined as zone G. For sheet drawing processes with a two-dimensional stress state generated within the flange material, flange material normally experiences a tensile stress in the material drawn-in direction and a compressive stress in the circumferential direction. Hence, zone G material located between grooves of tools

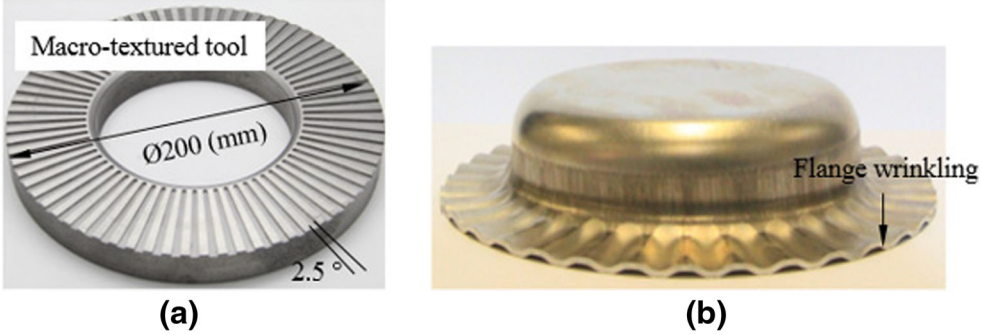

Fig. 1 Flange-wrinkling phenomenon for a two-dimensional stress state using a macro-textured tool design. **a** Macro-textured tool design. **b** Wrinkled part [12]

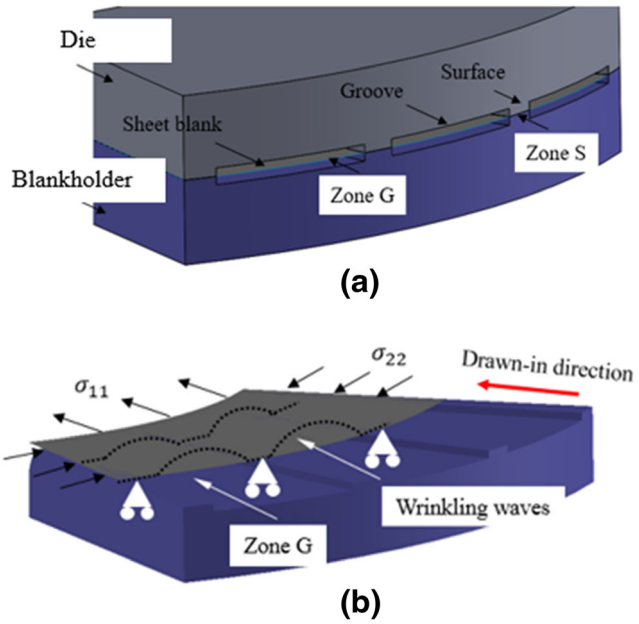

Fig. 2 Schematic illustration of macro-scale texture design and wrinkling concept. **a** Classification of texture features and sheet blank. **b** The mechanism of wrinkling occurrence

may buckle during draw-in as a result of the absence of blankholding force constraint, as shown in Fig. 2b.

According to the structure stability theory, buckling can be avoided when the structure dimension is controlled within a certain magnitude. Hence, dimensions of texture features need to be defined. A cylindrical deep-drawing design was used as the fundamental case study for the establishment of the buckling model. In this study, surface textures were only modelled on the blankholder, whilst the surfaces of punch and die remained flat. Figure 3 shows the plane view of a quarter of the macro-textured blankholder. The narrow sectors indicate surface and wide sectors indicate groove. Since the length scale (radial direction) of the groove is parallel to material flow direction which has no significant effect on flange wrinkling, the length-scale effect was ignored in this paper. The sizes of surface and groove of textures were defined by the subtended radial angles. Arc angles, θ_S and θ_G, of texture features were used, respectively, as shown in Fig. 3. The surface arc angle θ_S was fixed at 2.5°. Then, a normalised ratio reflecting the texture feature variation is defined as in Eq. (1).

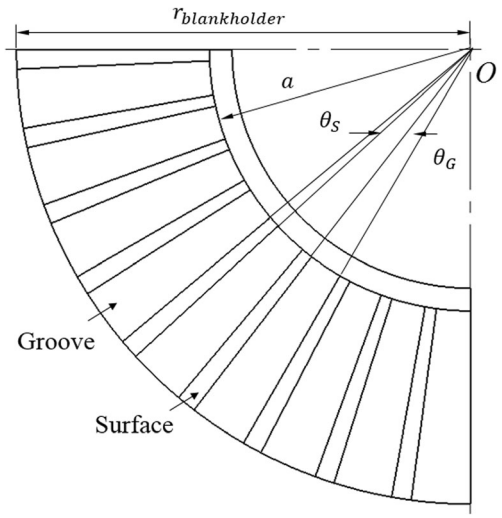

Fig. 3 A plane view drawing of macro-textured blankholder used for cylindrical deep drawing

$$\alpha = \theta_S/(\theta_S + \theta_G) \tag{1}$$

2.2 Constitutive equations of elastic-plastic solids

To model the buckling phenomenon of zone G flange material which is plastically deformed at room temperature, constitutive relationships of elastic-plastic solids need to be obtained. The incremental total strain can be expressed as the sum of elastic and plastic strain in a tensor expression as in Eq. (2) [18].

$$d\varepsilon_{ij} = d\varepsilon_{ij}^{e} + d\varepsilon_{ij}^{P} \tag{2}$$

where $d\varepsilon_{ij}$ represents the total strain increment and $d\varepsilon_{ij}^{e}$ and $d\varepsilon_{ij}^{P}$ represent the elastic strain increment and plastic strain increment, respectively.

The elastic strain increment is given in the generalised Hooke's law, described by Eq. (3), written using Einstein's index notation. In this equation, E and v are the Young's modulus and Poisson's ratio, respectively. Parameter δ_{ij} is the Kronecker delta ($\delta_{ij}=1$, if $i=j$ or $\delta_{ij}=0$ if $i\neq j$).

$$d\varepsilon_{ij}^{e} = \left[(1+v)d\sigma_{ij} - v d\sigma_{kk}\delta_{ij}\right]/E \tag{3}$$

The plastic stress increment is given by Hill's theory [19] using the plastic potential $f(\sigma_{ij})$. In terms of the plastic loading, the plastic stress increment is given in Eq. (4).

$$d\varepsilon_{ij}^{P} = H\frac{\partial f(\sigma_{ij})}{\partial \sigma_{ij}}df \tag{4}$$

where H is a scalar factor associated with deformation history, material stress state and work hardening given as Eq. (5) [20].

$$H = \frac{1}{E_T} - \frac{1}{E} \tag{5}$$

where in this equation, E_T is the tangent Young's modulus. The magnitude of E_T equals to the instantaneous slope of the effective stress-strain curve given in Eq. (6).

$$E_T = d\sigma_e/d\varepsilon_e \tag{6}$$

where σ_e is the effective stress and ε_e is the effective strain.

Substituting Eqs. (3)–(6) into Eq. (2), the constitutive relationship between the stress and strain increments in

the plastic loading is fully defined and expressed in Eq. (7).

$$d\varepsilon_{ij} = \frac{1}{E}\left[(1+\nu)d\sigma_{ij} - \nu d\sigma_{kk}\delta_{ij}\right] + \left(\frac{1}{E_T} - \frac{1}{E}\right)\frac{\partial f(\sigma_{ij})}{\partial \sigma_{ij}}\frac{\partial f(\sigma_{kl})}{\partial \sigma_{kl}}d\sigma_{kl} \quad (7)$$

With regard to sheet-stamping processes, the plane stress state normally applies $\sigma_{33} = 0$. By applying the principal stress state, an explicit expression of Eq. (7) can be obtained for a particular plastic potential $f(\sigma_{ij})$ and is given in Eq. (8).

$$d\varepsilon_{ij} = \begin{Bmatrix} d\varepsilon_{11} \\ d\varepsilon_{22} \\ d\varepsilon_{33} \end{Bmatrix} = \begin{Bmatrix} \left[\frac{1}{E} + \left(\frac{1}{E_T} - \frac{1}{E}\right)\left(\frac{\partial \sigma_f}{\partial \sigma_{11}}\right)^2\right] d\sigma_{11} + \left[\frac{-\nu}{E} + \left(\frac{1}{E_T} - \frac{1}{E}\right)\left(\frac{\partial \sigma_f}{\partial \sigma_{11}}\right)\left(\frac{\partial \sigma_f}{\partial \sigma_{22}}\right)\right] d\sigma_{22} \\ \left[\frac{-\nu}{E} + \left(\frac{1}{E_T} - \frac{1}{E}\right)\left(\frac{\partial \sigma_f}{\partial \sigma_{11}}\right)\left(\frac{\partial \sigma_f}{\partial \sigma_{22}}\right)\right] d\sigma_{11} + \left[\frac{1}{E} + \left(\frac{1}{E_T} - \frac{1}{E}\right)\left(\frac{\partial \sigma_f}{\partial \sigma_{22}}\right)^2\right] d\sigma_{22} \\ \frac{-\nu}{E}(d\sigma_{11} + d\sigma_{22}) \end{Bmatrix} \quad (8)$$

In this paper, two classical yield criteria applicable for isotropic materials, the von Mises and Tresca yield criteria, are considered due to the isotropic nature of the material resulting from the annealing heat treatment performed for the test-piece material. In addition, the selection of isotropic yield criteria can simplify the calculation significantly.

2.2.1 The von Mises yield criterion

The classical von Mises yield criterion yield function is given in Eq. (9).

$$J2 = \sigma_f^2/3 \quad (9)$$

where $J2 = [(\sigma_{11} - \sigma_{22})^2 + (\sigma_{22} - \sigma_{33})^2 + (\sigma_{11} - \sigma_{33})^2]/6$ for the principal stress states.

For the plane stress state cases, $\sigma_{33} = 0$, Eq. (9) can be further modified to Eq. (10).

$$\sigma_{11}^2 - \sigma_{11}\sigma_{22} + \sigma_{22}^2 - \sigma_f^2 = 0 \quad (10)$$

Considering the fundamental constitutive equation of an elastic-plastic solid, Eqs. (11) and (8) can be simplified and expressed as in Eq. (12).

$$d\varepsilon_{ij} = D_{ijkl}d\sigma_{kl} \quad (11)$$

$$d\varepsilon_{ij} = \begin{Bmatrix} d\varepsilon_{11} \\ d\varepsilon_{22} \\ d\varepsilon_{33} \end{Bmatrix} = \begin{Bmatrix} D_{1111}d\sigma_{11} + D_{1122}d\sigma_{22} \\ D_{2211}d\sigma_{11} + D_{2222}d\sigma_{22} \\ D_{3311}d\sigma_{11} + D_{3322}d\sigma_{22} \end{Bmatrix} \quad (12)$$

where D_{ijkl} is the compliance moduli [20]. Through an inverse substitution of Eq. (11), the constitutive relationship Eq. (11) is transferred to Eq. (13). Equation (13) can be further extended to Eq. (14), where L_{ijkl} is the instant stiffness matrix.

$$d\sigma_{ij} = L_{ijkl}d\varepsilon_{kl} \quad (13)$$

$$d\sigma_{ij} = \begin{Bmatrix} d\sigma_{11} \\ d\sigma_{22} \\ d\sigma_{33} \end{Bmatrix} = \begin{Bmatrix} L_{1111}d\varepsilon_{11} + L_{1122}d\varepsilon_{22} \\ L_{2211}d\varepsilon_{11} + L_{2222}d\varepsilon_{22} \\ L_{3311}d\varepsilon_{11} + L_{3322}d\varepsilon_{22} \end{Bmatrix} \quad (14)$$

For simplicity, the stiffness moduli are simplified as follows: $D_{1111} = D_{11}$, $D_{1122} = D_{2211} = D_{12} = D_{21}$, $D_{2222} = D_{22}$, $L_{1111} = L_{11}$, $L_{1122} = L_{2211} = L_{12} = L_{21}$ and $L_{2222} = L_{22}$.

Combining Eqs. (9), (10), (12) and (14), the detailed expressions of L_{ij} can be written as Eq. (15).

$$L_{ij} = \begin{Bmatrix} L_{11} \\ L_{22} \\ L_{12} \end{Bmatrix} = \begin{Bmatrix} \dfrac{1/E + H^* S_{22}^2/\sigma_f^2}{1/E^2 + H^*\left(S_{11}^2 + S_{22}^2\right)/\left(E\sigma_f^2\right) - 2\nu H^* S_{11}S_{22}/\left(E\sigma_f^2\right)} \\ \dfrac{1/E + H^* S_{11}^2/\sigma_f^2}{1/E^2 + H^*\left(S_{11}^2 + S_{22}^2\right)/\left(E\sigma_f^2\right) - 2\nu H^* S_{11}S_{22}/\left(E\sigma_f^2\right)} \\ \dfrac{\nu/E - H^* S_{11}S_{22}/\sigma_f^2}{1/E^2 + H^*\left(S_{11}^2 + S_{22}^2\right)/\left(E\sigma_f^2\right) - 2\nu H^* S_{11}S_{22}/\left(E\sigma_f^2\right)} \end{Bmatrix} \quad (15)$$

where S_{11} and S_{22} are the deviatoric stresses and $H^* = 9H/4$.

2.2.2 The Tresca yield criterion

Another classical isotropic yield criterion, for the plane stress state $\sigma_{33} = 0$, is that of Tresca yield criterion expressed by Eq. (16). It should be noted that the subscripts of the stress terms are arbitrarily defined instead of corresponding to the principal stress sequence. The sequence of principal stress is determined according to the specific metal-forming process.

$$\sigma_{11} - \sigma_{22} = \sigma_f \quad (16)$$

In a similar way, combining Eq. (16) with Eqs. (10), (12) and (14), the expression of the stiffness moduli using the Tresca yield criterion can be written as Eq. (17).

$$L_{ij} = \begin{Bmatrix} L_{11} \\ L_{22} \\ L_{12} \end{Bmatrix} = \begin{Bmatrix} \dfrac{E^2}{2E(1-\nu)-E_T(1-\nu^2)} \\ \dfrac{E^2}{2E(1-\nu)-E_T(1-\nu^2)} \\ \dfrac{E^2-EE_T(1-\nu)}{2E(1-\nu)-E_T(1-\nu^2)} \end{Bmatrix} \tag{17}$$

2.3 Material modelling in cold-forming condition

To obtain instant magnitudes of the above stiffness moduli and material flow stress at different stages of draw-in, a material model of a selected material is required. In this paper, a physical-based, dislocation-driven material model is applied [21]. The list of equations is given below from Eqs. (18)–(23).

$$\dot{\varepsilon}^P = \left(\frac{\sigma/(1-\omega)-R-k}{K}\right)^{n_1} \tag{18}$$

$$\dot{R} = 0.5B\bar{\rho}^{-0.5}\,\dot{\bar{\rho}} \tag{19}$$

$$\dot{\bar{\rho}} = A(1-\bar{\rho})|\dot{\varepsilon}_P| - C\bar{\rho}^{n_2} \tag{20}$$

$$\dot{\omega} = \eta_1 \frac{\left|\dot{\varepsilon}^P\right|^{\eta_2}}{(1-\omega)^{\eta_3}} \tag{21}$$

$$\sigma = (1-\omega)E\left(\varepsilon-\varepsilon^P\right) \tag{22}$$

Equation (18) is the traditional power law viscoplastic flow formulation considering damage effect ω on viscoplastic flow. Parameter $\dot{\varepsilon}^P$ represents the plastic strain rate, k is the initial yield stress, R is the hardening stress and ω is the factor reflecting damage. Equation (19) represents the evolution of material-hardening R, which is governed by the evolution of normalised dislocation density $\bar{\rho}$. Parameter $\bar{\rho}$ is equal to $(\rho-\rho_i)/\rho_m$, ρ_i is the initial material dislocation density and ρ_m is the maximum dislocation density. Equation (21) represents the damage evolution for the uniaxial formulation, which is a function of plastic strain rate $\dot{\varepsilon}^P$. Equation (22) is the Hooke's law for a simple uniaxial state. Details of the illustration of each equation are given by Lin et al. [22]. The material constants of this dislocation-driven material model can be determined using uniaxial tensile experiments of a particular alloy. Then, such a material model can be used for both developing the buckling model and numerical simulations via user-defined subroutine.

2.4 Bifurcation function

To overcome the inaccuracy of reduced modulus used in beam and plate buckling models, the bifurcation function proposed by Hutchinson et al. [16] was utilised. In addition, zone G material can be considered as a quasi-shallow shell, as defined in DMV shell theory. This shell is thought to be accurate when the texture hollow, groove, is sufficiently large, whilst the assumption may not be accurate for small texture designs which need to be further validated using experiments. Hence, the accurate application range of the DMV shell theory assumption needs to be validated experimentally. Before experiencing deformation, the assumed shell is believed to remain as a relatively flat geometry, and the displacement components are varying functions of the coordinates. The bifurcation function described in Eq. (23) is utilised here to evaluate buckling occurrence for the zone G material [16]. In this paper, as the flange material experiences plastic deformation when drawn in, the wrinkling of the zone G material is assumed to be plastic buckling.

$$\begin{aligned} F &= \iint \frac{t^3}{12} L_{ijkl}\kappa_{ij}\kappa_{kl}ds + \iint tL_{ijkl}\varepsilon^s_{ij}\varepsilon^s_{kl}ds + \iint t\sigma_{ij}w_{,i}w_{,j}ds \\ &= F_b + F_m + F_n \end{aligned} \tag{23}$$

where L_{ijkl} is the incremental stiffness matrix related to stress increments as mentioned above, κ_{ij} is the incremental bending strain, ε^s_{ij} is the incremental stretching strain, σ_{ij} is the in-plane principal stresses, w_i is the displacement increment of buckling with a direction normal to the shell middle surface and s denotes the area of the shell middle surface over which wrinkles occur. The bifurcation function can be divided into three terms for simplicity, where F_b represents the bending strain energy term, F_m represents the membrane stress term and F_n represents the potential energy of the edge stress. In terms of this function, when $F>0$ for all admissible fields, bifurcation will not occur and buckling cannot happen. Whilst for $F=0$, bifurcation becomes possible, indicating experiencing buckling for some non-zero fields [16].

2.4.1 Incremental strain and stress

According to the basic relationships of the DMV shell theory, incremental bending and stretching strains due to buckling from the uniform membrane state can be calculated using Eqs. (24) and (25) [13],

$$\kappa_{ij} = -w_{,ij} \tag{24}$$

$$\varepsilon^s_{ij} = \left(u_{i,j} + v_{j,i}\right)/2 \tag{25}$$

where w is the mathematical expression of deflection and u,v represents the in-plane displacement fields.

Considering the geometry feature of cylindrical cup deep-drawing process, a cylindrical coordinate system (r θ z) is established. Then, the displacement fields become functions of instant radius r and polar angle θ, which are $u(r,\theta)$, $v(r,\theta)$ and $w(r,\theta)$ for this cylindrical coordinate system. Substituting the displacement fields into Eqs. (24) and (25), the detailed expressions of incremental strains are given in Eqs. (26) and (27).

$$\kappa_{ij} = \begin{Bmatrix} \kappa_{rr} \\ \kappa_{\theta\theta} \\ \kappa_{r\theta} \end{Bmatrix} = \begin{Bmatrix} -\dfrac{\partial^2 w(r,\theta)}{\partial r^2} \\ -\dfrac{1}{r}\dfrac{\partial w(r,\theta)}{\partial r} - \dfrac{1}{r^2}\dfrac{\partial^2 w(r,\theta)}{\partial \theta^2} \\ -\dfrac{1}{r}\dfrac{\partial^2 w(r,\theta)}{\partial r \partial \theta} + \dfrac{1}{r^2}\dfrac{\partial w(r,\theta)}{\partial \theta} \end{Bmatrix} \tag{26}$$

$$\varepsilon^s_{ij} = \begin{Bmatrix} \varepsilon^s_{rr} \\ \varepsilon^s_{\theta\theta} \\ \varepsilon^s_{rs} \end{Bmatrix} = \begin{Bmatrix} \dfrac{\partial u(r,\theta)}{\partial r} \\ \dfrac{u(r,\theta)}{r} + \dfrac{1}{r}\dfrac{\partial v(r,\theta)}{\partial \theta} \\ \dfrac{1}{2}\left[\dfrac{1}{r}\dfrac{\partial u(r,\theta)}{\partial \theta} + \dfrac{\partial v(r,\theta)}{\partial r} - \dfrac{v(r,\theta)}{r}\right] \end{Bmatrix} \tag{27}$$

The incremental stress resultants N_{ij} and bending moments M_{ij} at buckling can be calculated using the above incremental strains. These resultants are given by Eqs. (28) and (29).

$$N_{ij} = tL_{ijkl}\varepsilon^s_{kl} \tag{28}$$

$$M_{ij} = t^3 L_{ijkl}\kappa_{kl}/12 \tag{29}$$

In terms of the in-plane stress components, the tensile and compressive stresses of the flange in cylindrical deep-drawing process are normally expressed in Eqs. (30) and (31), respectively, when neglecting the friction term due to the non-blankholding force constraint of zone G [23].

$$\sigma_{rr} = \sigma_f \ln(b/r) \tag{30}$$

$$\sigma_{\theta\theta} = \sigma_f [\ln(b/r) - 1] \tag{31}$$

where σ_f is the material flow stress, b is the outside flange radius and r is the instant flange radius for a selected infinitesimal small unit.

2.4.2 Boundary conditions

To obtain analytical expressions for the above incremental strains, mathematical functions using different boundary condition of the displacement fields are required. Selecting a vertical cross-section view of one unit (two surfaces and one groove) for tool textures, Fig. 4 shows the schematic illustrations of (a) the hinged and (b) the inbuilt boundary conditions [24]. Each zone G material clamped by tools located above groove and between two adjacent surfaces can be assumed as a shell sector with constraints at two ends. Zheng et al. [12] has established the mathematical expressions of deflections for zone G material based on the above boundary conditions utilising a geometry assumption of two-dimensional plate; a detailed discussion and demonstration of the accuracy of the expressions were also described. The inbuilt boundary condition represents a fully clamped tool constraint at an extremely high blankholding force; however, this kind of blankholding force may increase the radial stress severely, and the material cannot be drawn in. Regarding the hinged boundary condition, sheet metal can be drawn into the die with no displacement in the vertical direction, $w(r,\theta)|_{\theta=0} = 0$ and $w(r,\theta)|_{\theta=\theta_G} = 0$, which means that wrinkling will not occur for zone S material. The mathematical equations for deflection curves of hinged and inbuilt boundary condition are given in Eqs. (32) and (33), respectively. The in-plane displacements to calculate the stretching strains are given in Eq. (34) [13]. During material draw-in, it is assumed that zone G material has no flow in the hoop direction, $u(r,\theta)|_{\theta=0} = 0$ and $u(r,\theta)|_{\theta=\theta_G} = 0$, whilst the zone G can be drawn into the die when the radial displacement is non-zero [13].

$$w(r,\theta) = \delta_1 (r - a)\sin(n\pi\theta/\theta_G) \tag{32}$$

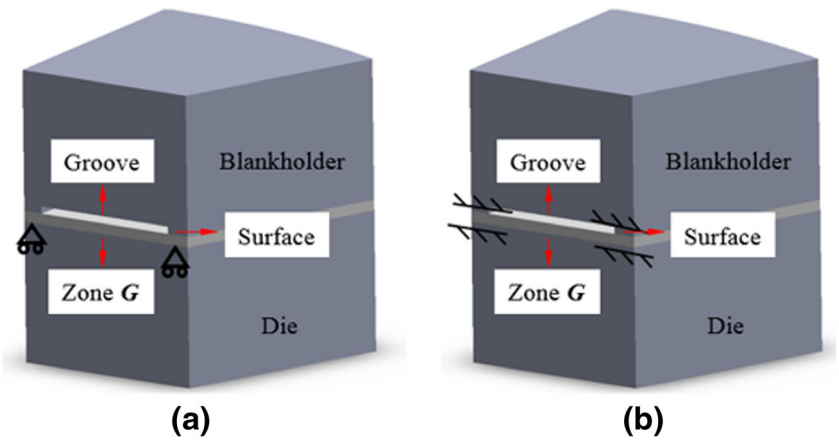

Fig. 4 Schematic illustrations of boundary condition. **a** The hinged. **b** The inbuilt [12]

$$w(r,\theta) = \delta ln_1(r-a)[\cos(2n\pi\theta/\theta_G)-1] \tag{33}$$

$$\begin{cases} u(r,\theta) = \delta_2 r\cos(n\pi\theta/\theta_G) \\ v(r,\theta) = \delta_3 r\sin(n\pi\theta/\theta_G) \end{cases} \tag{34}$$

where δ_1 and n are the wave amplitude and numbers δ_2 and δ_3 are the constants. All of these displacement fields are functions of instantaneous radius r and the polar angle θ. The units of displacement fields are consistent with the radius r in millimetre.

2.5 Wrinkling determination

2.5.1 The criterion of wrinkling occurrence

The wrinkling occurrence using this bifurcation function is defined when $F=0$. Considering the plane stress feature of sheet metal processes, Eq. (23) is further extended and expressed in Eq. (35) for a particular zone G material, and the bifurcation is expressed by three parts, F_b, F_m and F_n, as given by Eq. (35).

$$\begin{cases} F_b = \frac{1}{2}\int_0^{\theta_G}\int_a^r \left\{ \frac{t^3}{12}\left[L_{11}\kappa_{rr}\kappa_{rr} + 2L_{12}\kappa_{rr}\kappa_{\theta\theta} + L_{22}\kappa_{\theta\theta}\kappa_{\theta\theta} + 4L_{44}\kappa_{r\theta}\kappa_{r\theta}\right] \right\} rdrd\theta \\ F_m = \frac{1}{2}\int_0^{\theta_G}\int_a^r \left\{ t\left[L_{11}\varepsilon^s_{rr}\varepsilon^s_{rr} + 2L_{12}\varepsilon^s_{rr}\varepsilon^s_{\theta\theta} + L_{22}\varepsilon^s_{\theta\theta}\varepsilon^s_{\theta\theta} + 4L_{44}\varepsilon^s_{r\theta}\varepsilon^s_{r\theta}\right] \right\} rdrd\theta \\ F_n = \frac{1}{2}\int_0^{\theta_G}\int_a^r \left\{ t\left[\sigma_{rr}\left(\frac{\partial w}{\partial r}\right)^2 + \sigma_{\theta\theta}\left(\frac{1}{r}\frac{\partial w}{\partial \theta}\right)^2\right] \right\} rdrd\theta \end{cases} \tag{35}$$

As can be seen from the expressions for F_b and F_m, there exists a component L_{44}, which represents the induced shear stress component resulting from deformation. In deep-drawing processes, σ_{rr} and $\sigma_{\theta\theta}$ can be regarded as the principal stresses corresponding to σ_{11} and σ_{22} mentioned above. Chu and Xu [25] has concluded that this shear stress component is vitally important for predicting wrinkling occurrence. In this paper, it is assumed that $L_{44}=E/[2(1+\nu)]$ to conduct the calculation [13].

By combining the incremental strain expressions (Eqs. (26) and (27)) with the displacement fields (Eqs. (32)–(34)) and substituting them into Eq. (35), the bifurcation function can be rewritten in matrix form shown in Eq. (36). The critical condition of wrinkling occurrence is $F=0$, and hence, $Det|M|$ must be equal to 0. The magnitude of this determinant can be calculated as in Eq. (37).

$$F = \{\delta_1 \quad \delta_2 \quad \delta_3\} \begin{vmatrix} M_{11} & 0 & 0 \\ 0 & M_{22} & M_{23} \\ 0 & M_{32} & M_{33} \end{vmatrix} \begin{Bmatrix} \delta_1 \\ \delta_2 \\ \delta_3 \end{Bmatrix} \tag{36}$$

$$Det|M| = M_{11}\left(M_{22}M_{33} - M_{23}^2\right) \tag{37}$$

It can be calculated that $M_{22}M_{33}-M_{23}^2 \neq 0$. Hence, the only solution of this determinant is $M_{11}=0$. As the coefficient of M_{11} is δ_1, the bifurcation condition has no relationship with the coefficients of δ_2 and δ_3, which means that the effect of membrane stress can be neglected, and the bifurcation function is related only to F_b and F_n. Hence, an analytical expression of M_{11} can be obtained by integration of Eq. (35).

2.5.2 Calculation procedure

To capture the instant forming stage when flange wrinkling occurs, a relationship between the actual deep-drawing process and developed buckling model needs to established. In this study, a simple method [26] using the relationship between the hoop strain of flange material (actual forming process) and the corresponding stiffness matrix (buckling model) was applied, as shown in Fig. 5a. In this method, the outside edge of zone G material can be assumed as a uniaxially compressed slab ($\sigma_{rr}=0$) according to Eq. (30). Hence, the deformation type of this slab is assumed to be identical to a uniaxial compression test. In addition, the arc shape of material is assumed to remain unchanged during draw-in. When the flange material is drawn from the initial stage to a certain stage, the instant diameter reduction, Δ^i, defined in Eq. (38) corresponds to an effective strain of uniaxial stress-strain curve, as described in Eq. (39). Finally, the above relationship can be used to capture the onset of flange wrinkling during material draw-in.

$$\Delta^i = \left(b - r^i\right)/b \tag{38}$$

$$\varepsilon^i = \ln\left(1+\Delta^i\right) \tag{39}$$

Figure 5b illustrates the flowchart for computer-based determination of the occurrence of wrinkling during the forming process. This consists of the following steps:

1. Input a radius reduction Δr, calculating corresponding "effective strain" using Eqs. (38) and (39).
2. Obtain the instant tangent modulus E_t using dislocation-driven material model in Eq. (40), the plane stress state (σ_{rr}, $\sigma_{\theta\theta}$) and the corresponding displacement fields.

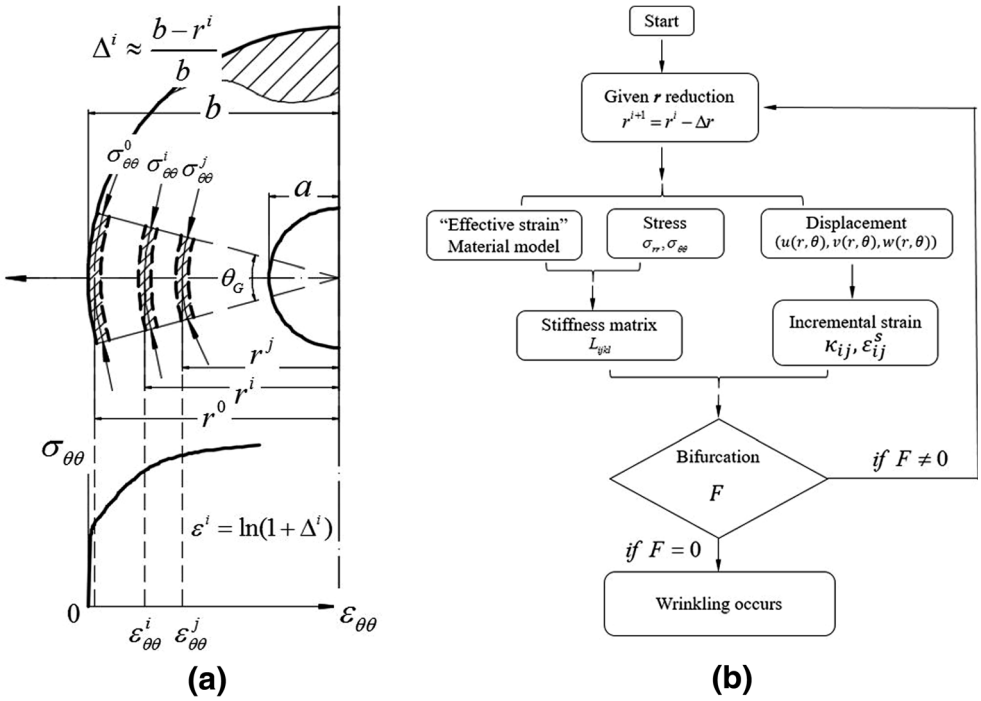

Fig. 5 Wrinkling determination. **a** The relationship between deep drawing and analytical buckling model. **b** The calculation procedure of flange wrinkling

3. Obtain the instant stiffness matrix L_{ijkl} and incremental strains κ_{ij} and ε^s_{ij} according to step (2) results.
4. Substitute stiffness matrix and incremental strains in the bifurcation function. If $F=0$, wrinkling occurs and output the critical radius value. If $F\neq 0$, return to step (2).

$$E_t = \frac{\sigma^{i+1} - \sigma^i}{\varepsilon^{i+1} - \varepsilon^i} \tag{40}$$

Recalling the stiffness matrix of the von Mises and Tresca yield criteria, Eqs. (15) and (17), it is impossible to obtain an analytical solution of the bifurcation function using Eq. (15). To simplify and enable calculation, due to wrinkles initiating at the outside flange with a maximum compressive hoop stress, the stiffness matrix of edge material of zone G can be used. Then the stress state becomes $(0 \quad 0 \quad \sigma_{\theta\theta})$, and $\sigma_{\theta\theta}$ equals to the effective stress. Thus, the stiffness moduli L_{ij} can be simplified to Eq. (41).

$$L_{ij} = \begin{Bmatrix} L_{11} \\ L_{22} \\ L_{12} \end{Bmatrix} = \begin{Bmatrix} \dfrac{3EE_T + E^2}{4(1-\nu^2)E_T + (E-E_T)(5+4\nu)} \\ \dfrac{4E^2}{4(1-\nu^2)E_T + (E-E_T)(5+4\nu)} \\ \dfrac{4\nu EE_T + 2\left(E^2 - EE_T\right)}{4(1-\nu^2)E_T + (E-E_T)(5+4\nu)} \end{Bmatrix} \tag{41}$$

In terms of $J2$ yield criterion, combining the displacement fields Eqs. (32)–(34) with the incremental strain expressions Eqs. (26)–(27), the mathematical expressions of incremental strains can be obtained for a particular coordinate $(r, \quad \theta)$. By substituting the incremental strains and stiffness matrix into the bifurcation function, an analytical expression of bifurcation function using the von Mises yield criterion can be obtained and used to determine the wrinkling occurrence. In a similar way, the analytical buckling model using Tresca yield criterion can also be established. Table 1 lists the process parameters needed for the model calculation.

3 Experimental validations of buckling model

3.1 Quasi-static uniaxial tensile test

Quasi-static uniaxial tensile tests were performed to obtain mechanical properties of test-piece material, AA6082. The as-received material was in T6 condition with a thickness of 1.5 mm, and the chemical composition is given in Table 2 [27]. The uniaxial tensile test specimens were designed according to the AMMS standard, and they were machined using laser cutting from raw material AA6082-T6 sheets at the rolling direction. Then, an annealing treatment, 415 °C for 1 h with subsequent furnace cooling, was performed on the specimen. The obtained tensile test results can be used to determine material constants of the buckling model in Sect. 2.3.

Table 1 The process parameters for model calculation

D_{punch} (mm)	v	E (MPa)	θ_s (deg)	n	Δr (mm)
100	0.33	70,000	2.5	1	0.1

Table 2 The main chemical composition of AA6082 [27]

Element	Mn	Fe	Mg	Si	Cu	Zn	Ti	Cr	Al
Percent	0.4–1.0	0.5	0.6–1.2	0.7–1.3	0.1	0.2	0.1	0–0.25	Balance

3.2 Deep-drawing test

Cylindrical deep-drawing test results as in the author's previous publication [12] were used here to validate the developed buckling model, as shown in Fig. 6a. Figure 6b shows the necessary tool dimensions for the calculation of the analytical buckling model. The test-piece material used throughout the deep-drawing tests was the same as the uniaxial tensile tests. Texture features were only machined on the blankholders. Different texture ratios were used, $\alpha = 1$, 1/4 and 1/6, for the deep-drawing tests. The blankholding forces used were 10 and 40 kN, and the forming speed was 75 mm/s. All the tests were performed in cold-stamping condition with the use of Omega-35 lubricant.

4 FE simulation analysis

4.1 FE simulation programme

The minimal texture ratio reflecting the largest groove in experimentations was 1/6, of which FE simulations were performed. Additional simulations were computed for existing and theoretical texture ratios, $\alpha = 1$, 1/4, 1/6, 1/8 and 1/10, utilising PAM-STAMP. Figure 7 shows the FE model of cylindrical deep drawing, as well as the loading and boundary conditions. The dimensions of tools were consistent with experimental setups. The mesh of blank is extremely important for guaranteeing the accuracy of simulation [28]. In this study, the mesh of test-piece material was selected as shell element, Belytschko-Tsay, with a fixed size at 4 mm. For different draw ratios, the number of test-piece elements was 3456, 4012 and 4320, respectively, which were sufficiently large to guarantee simulation accuracy. The mesh size was fine enough for utilising subroutine in PAM-STAMP software as numerically determined. Five integration points at the mid-plane of the element were used. The tool mesh was default solid elements and treated as rigid bodies. Table 3 lists the computation conditions for FE simulations. All the simulations were performed in cold-stamping condition.

4.2 Material modelling

The developed dislocation-driven material model of AA6082 in Sect. 2.3 was validated by the uniaxial tensile test result in Sect. 3.1. The test-piece material was considered as isotropic after annealing treatment, and only mechanical data (stress-strain) in the rolling direction was used. Figure 8a shows the comparisons between experimental results and material model predictions. The symbols represent the experimental data of the uniaxial tensile test, and the solid lines represent the fittings of material model using three different strain rates. As can be seen in this figure, the level of flow stress can be regarded to be independent of strain rate, which is consistent with elastic-plastic mechanism of aluminium alloy in cold-stamping condition. A good agreement was obtained indicating that the developed material is capable of reflecting material deformation in deep-drawing process. Table 4 lists the material constants of the dislocation-driven material model. The material model was implemented into the FE simulations via user-defined subroutine. Typical computed contours were shown in Fig. 8b.

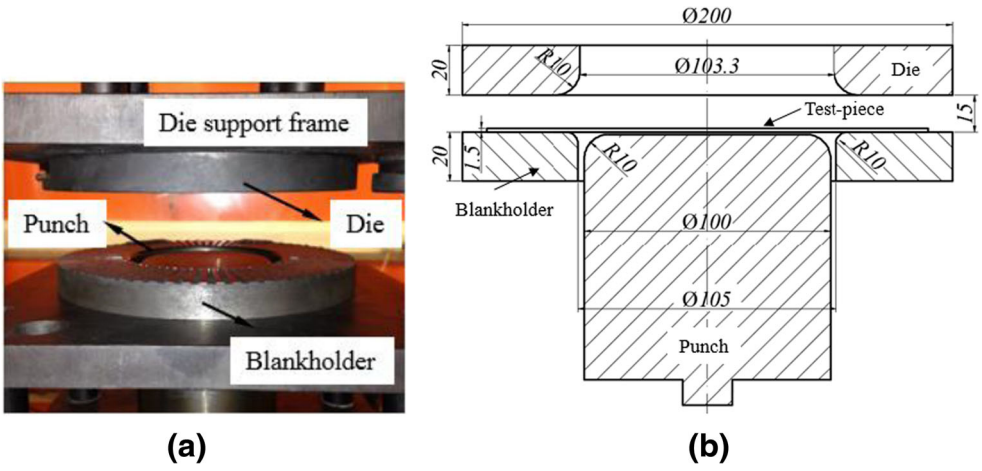

Fig. 6 Experimental setup details. **a** Deep-drawing tool set. **b** Tool dimensions (all dimensions are in millimetre)

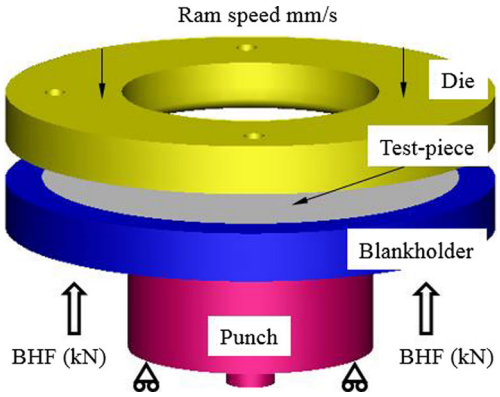

Fig. 7 The finite element model of cylindrical deep drawing

4.3 FE model verification

Figure 9 shows the validation of the FE model using the comparison of normalised thickness distribution $\bar{t}$ defined in Eq. (42) between experimentational results and simulations using a non-textured blankholder, $\alpha = 1$, for different test-piece draw ratios. Figure 9a shows a sectioned view of the formed part through a plane along the rolling direction through the centre of bottom cup surface. Considering the symmetric feature of the formed component, experimental data indicated by solid symbols were measured only on half of the cup using digital callipers at positions shown in Fig. 9a. Corresponding predicted values of FE simulations indicated by solid lines were output to compare to this data, as shown in Fig. 9b. A close agreement was found between experimentations and simulations. Hence, it can be concluded that the developed FE model with the implemenation of material model via user-defined subroutine is capable of investigating the wrinkling phenomenon and material deformation and validates the established buckling model further.

$$\bar{t} = t/t_0 \tag{42}$$

where t is the measured or predicted thickness at a particular position and t_0 is the initial test-piece thickness.

Table 3 Computation conditions

Computional condition	Magnitudes
Blankholding force (kN)	10, 40
Interfacial friction coefficient	0.09
Forming speed (mm/s)	75
Texture ratio	1, 1/4, 1/6, 1/8 and 1/10
Test-piece draw ratio	1.7, 1.8 and 1.9

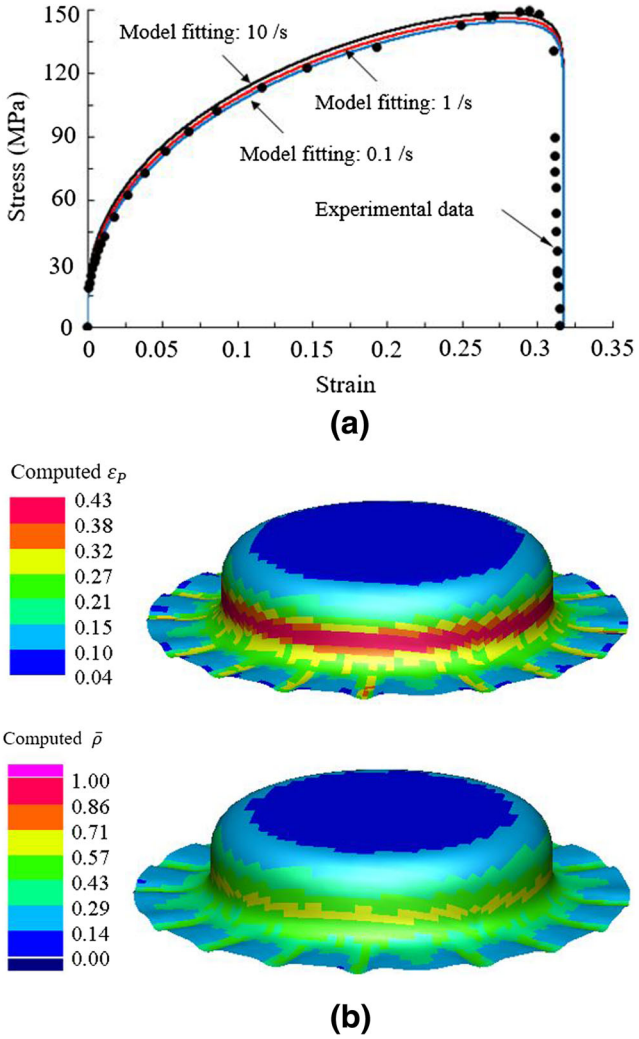

Fig. 8 Material modelling in FE simulation. **a** Material model fitting. **b** Typical computational results of user-defined subroutine

4.4 Wrinkling occurrence definition

Figure 10 gives the experimental and numerical definitions of the onset of zone G wrinkling. The onset of wrinkling is defined when the height between the peak and lowest points of wrinkles reaches 1 mm. However, the occurrence of wrinkling is difficult to be captured precisely considering the stroke fluctuations of the hydraulic press ram and uncertainties in the measurement. However, such a limitation can be overcome using a numerical approach, as shown in Fig. 10b. In

Table 4 Material constants of AA6082 material model

K (MPa)	k (MPa)	B (MPa)	E (MPa)	n_2
9	5.1	220	70,000	1.8
A	C	η_1	η_2	η_3
2.15	0	0.15	20	1

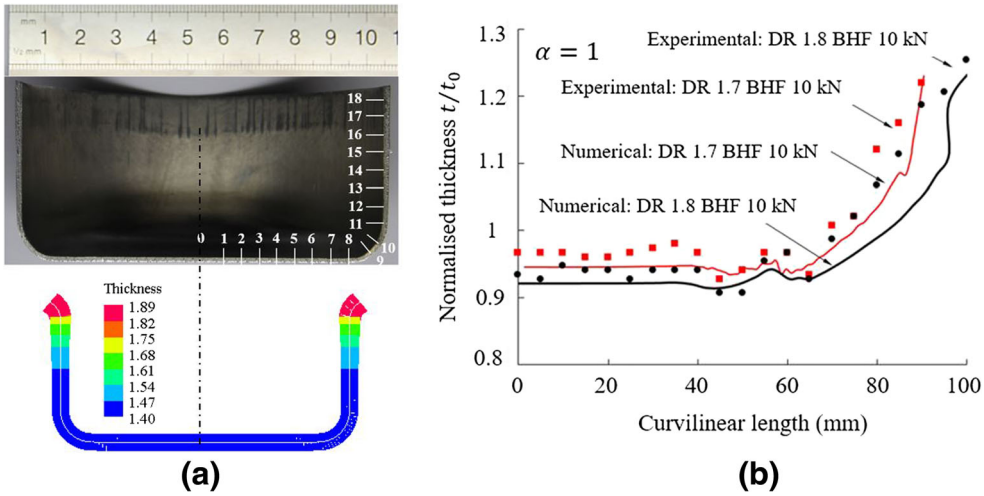

Fig. 9 FE model validation. **a** Section view of FE model validation. **b** The comparison of normalised thickness distribution, where *symbols* represent the experimental data and *lines* represent the computational data

this figure, r^i indicates the instantaneous flange radius when the test piece experienced flange wrinkling.

5 Results and discussions

5.1 Boundary condition assumption

The mathematical expressions of wrinkles which determine the incremental strain tensors are different using different boundary condition assumptions, in Eqs. (32) and (33). Figure 11 shows the effects of different boundary conditions on the prediction accuracy of the established buckling model. The comparison of test-piece radius reduction when wrinkling occurred between the experimental and analytical results is shown. For the figure, the selected texture ratio was $\alpha = 1/6$ at a forming speed of 75 mm/s. The hollow square symbols represent the blankholding force 10 kN, and the solid square symbols represent the blankholding force 40 kN. The yield function used was the von Mises for the analytical buckling models. As can be seen in this figure, with the utilisation of hinged boundary condition, good agreement can be found between the buckling model (solid lines) with the experimental results (symbols). Whilst in terms of the inbuilt boundary condition (dash line), no wrinkling occurrence was detected, which implies that the initial test piece can be entirely drawn in analytically. However, wrinkling was easily generated for zone G at the flange when test-piece diameter reduction was small according to the experimental observations. Hence, it can be concluded that the inbuilt boundary condition over-predicted the resistance of wrinkling in the flange. The actual surface constraint of zone G material is closer to the hinged boundary condition. In addition, Fig. 11 also illustrated the blankholding force effects on the flange-wrinkling occurrence. From the experimental results, different blankholding force magnitudes, 10 and 40 kN, have very limited effects on the flange-wrinkling occurrence, although with increasing blankholding force (BHF), the resistance of wrinkling is increased and the increased extent is very small and largely negligible. Theoretically, wrinkling can be avoided using a sufficiently great BHF. The sufficiently great BHF constraint can be reflected in the boundary condition assumption of inbuilt in the analytical model, which also predicted the non-wrinkling and further verified the accuracy of modelling. However, such a great blankholding force is unrealistic in actual forming processes, as it might cause fracture due to induced high radial tensile stresses.

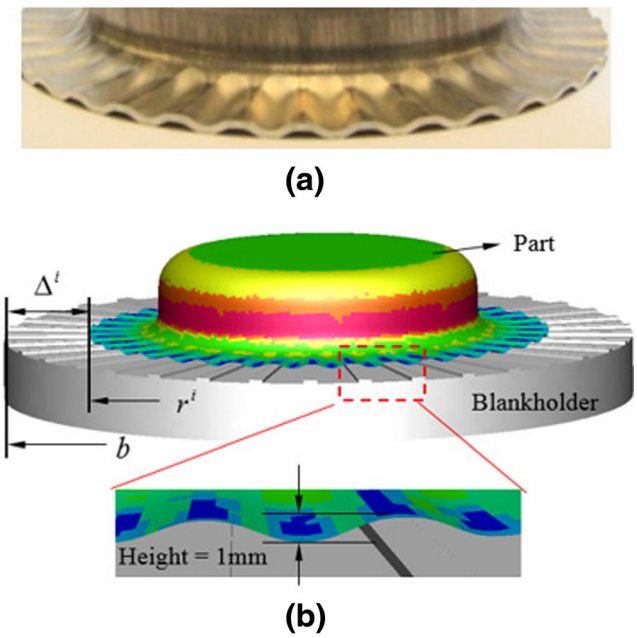

Fig. 10 Wrinkling occurrence. **a** Experimental observation. **b** Numerical definition

5.2 Yield function effect

The stiffness matrix used in the bifurcation function depends on the chosen yield criterion. Figure 12 shows the

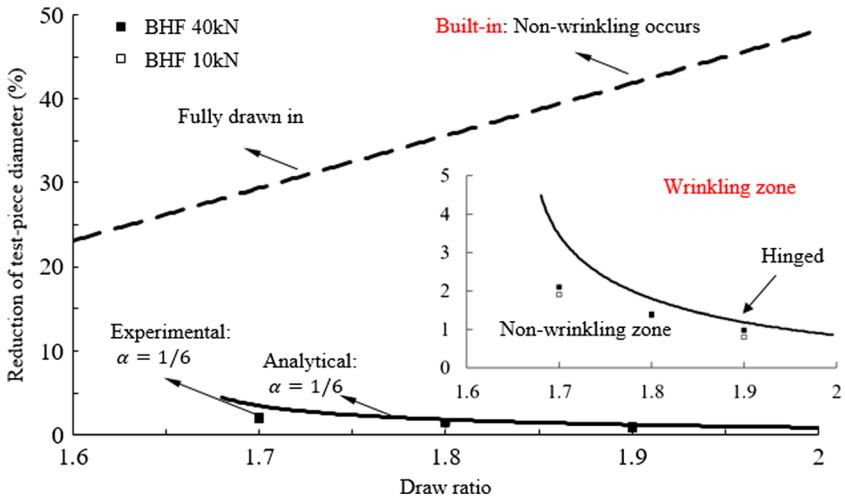

Fig. 11 Effect of boundary condition assumption on the buckling model prediction accuracy using BHF 10 and 40 kN at a forming speed of 75 mm/s

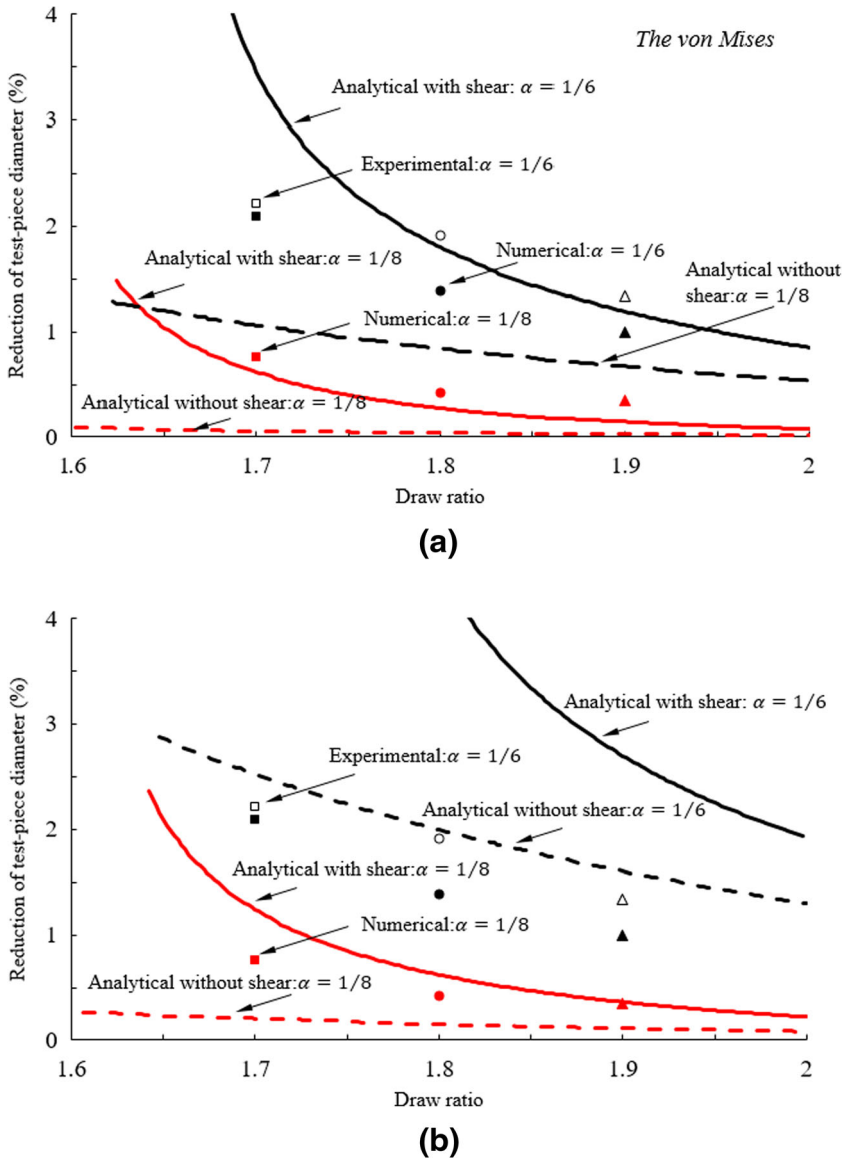

Fig. 12 Yield function effect on the flange buckling model. **a** The von Mises. **b** The Tresca for texture ratios $\alpha = 1/6$ and $\alpha = 1/8$ at a blankholding force 10 kN and forming speed of 75 mm/s

comparisons of typical experimental ($\alpha = 1/6$), further numerical ($\alpha = 1/6$ and $\alpha = 1/8$) results and analytical predictions of flange-wrinkling occurrence for the two yield criteria: (a) the von Mises and (b) the Tresca, for a 10-kN BHF and a forming speed of 75 mm/s. The square, circular and triangular symbols represent the draw ratios of 1.7, 1.8 and 1.9, respectively. The induced shear strain components are calculated for both yield criteria. As can be seen in this figure, the analytically predicted results without shear (dashed lines) are much lower than the experimental results (hollow symbols) and numerical results (solid symbols), and large differences can be observed. However, after the inclusion of induced strain term, the analytical predicted results with shear (solid lines) have much less variation with the experimental results and numerical results, especially for the larger texture ratio case, $\alpha = 1/8$. For the Tresca yield function in Fig. 12b, there is some difference between the model calculations and experimentations for a texture design, $\alpha = 1/6$, whilst closer agreement can be found in Fig. 12a using the von Mises yield criterion. In general, the analytical buckling model using Tresca yield criterion has a higher prediction than using the von Mises yield criterion. Whilst when the texture ratio becomes greater, both yield criteria have good capabilities to predict the onset of wrinkling within reasonable errors.

5.3 Application range of buckling model

As discussed above, the analytical buckling model was established on the assumption of DMV shell theory of zone G material, which is believed to be more accurate for large texture features. The geometry of zone G material was determined by texture ratio and test-piece draw

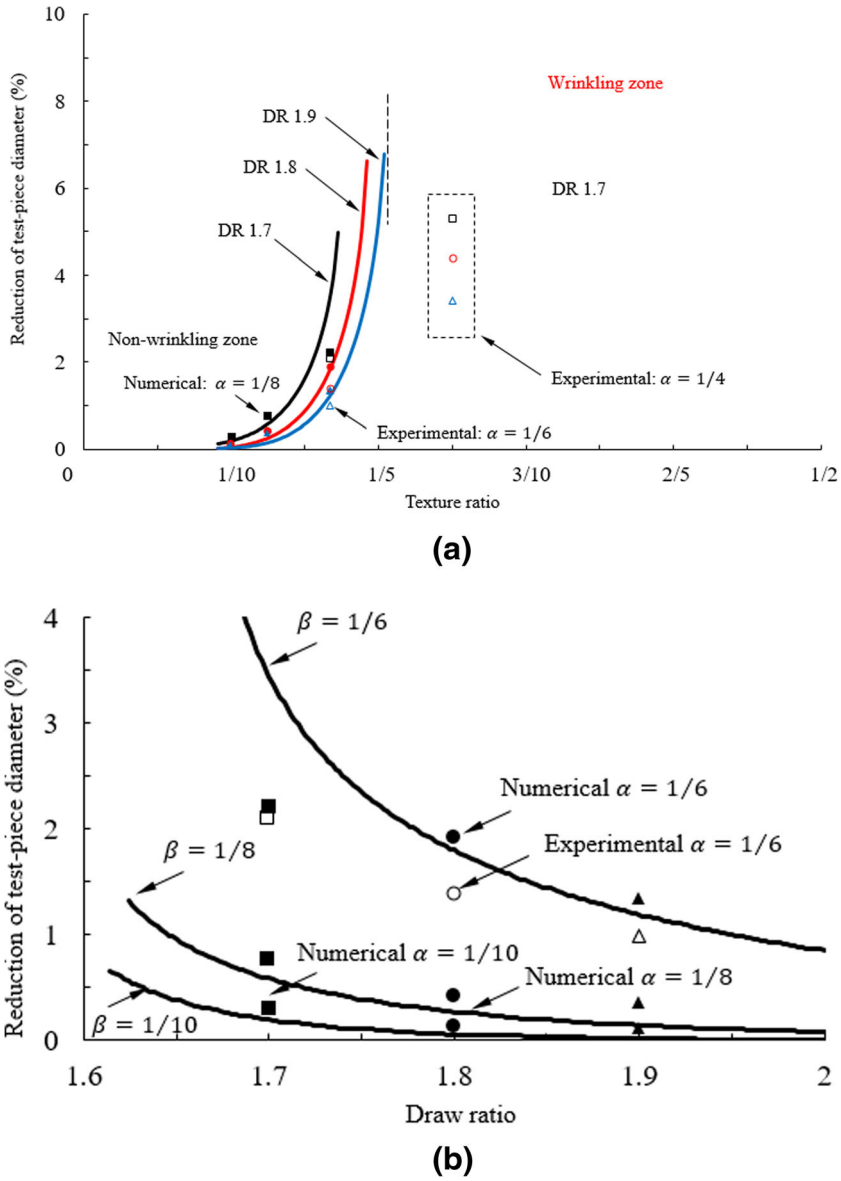

Fig. 13 Application ranges of buckling models. **a** Different texture ratio. **b** Different draw ratio

ratio. Figure 13a shows the wrinkling occurrence of zone G material for different draw ratios using different tool texture ratio. The solid lines represent the analytical buckling model predictions for different draw ratios, whilst the solid symbols represent the numerical results obtained at a blankholding force of 10 kN and a forming speed of 75 mm/s, where the square, circle and triangle shapes represent 1.7, 1.8 and 1.9 of used draw ratio, respectively. The hollow symbols represent the experimental results using texture ratio 1/4. Good agreements can be observed between numerical predictions and analytical buckling results for smaller texture ratios (larger zone G area), $\alpha = 1/6, 1/8$ and 1/10. However, there exists a great difference between analytical lines and experimental symbols for a relatively larger texture ratio, $\alpha = 1/4$, which implies that wrinkling cannot be predicted using this buckling model for smaller feature textured surfaces. The reason for this big difference is due to the DMV shell theory assumption. If the area of unsupported material (zone G) is small, then the test-piece thickness is relatively larger and the zone G is not accurate to be assumed as a shell. In comparison, the buckling models based on beam and plate assumptions proposed by Zheng et al. [12] enable the prediction of such wrinkling phenomena for a small texture design. Similar results have been found between those models and the current one for the texture design, $\alpha = 1/6$. However, the previous models were believed to be inaccurate in reflecting the geometry effects of large texture features. Another important factor affecting wrinkling is the test-piece draw ratio. Figure 13b shows the wrinkling occurrence of zone G material using different test-piece draw ratio. The solid lines represent the results from the analytical buckling model-predicted results using the hinged boundary condition and the von Mises yield criterion, whilst the square symbols represent the experimental results using a tool texture ratio of $\alpha = 1/6$ at a blankholding force of 10 kN. The forming speed used was 75 mm/s. The circular symbols represent further validated numerical results using a series of texture ratios $\alpha = 1/6$, 1/8, 1/10 to minimise the experimental tests. With increasing draw ratio, the critical reduction of test-piece diameter decreases, which means that at a given texture ratio, the deep-drawing process with a large draw ratio is easier for wrinkling to occur. The reason is similar to that of texture ratio effect; that is, the wider unsupported flange arising with larger diameter blanks is less resistant to buckling. Most of the numerical results are higher than analytical results for the three large tool textures. One possible reason for this may be due to the wrinkling determination in the simulation. Wrinkling occurrence is defined when the largest height difference reaches 1 mm. However, the wrinkling occurrence detected in the analytical buckling model may be earlier than that defined in the numerical simulation. Based on above discussions, the application range of developed buckling model is for smaller texture ratios at least lower than 1/6 and larger draw ratios.

6 Conclusions

In this paper, an advanced buckling model that can be used to predict flange-wrinkling behaviour in sheet-stamping processes with the utilisation of textured tool surfaces was established. A series of classic mechanic theories, such as bifurcation and DMV theories, are integrated in this buckling model with advanced dislocation-driven based material model. Experimental and numerical approaches were used to validate the accuracy of the proposed buckling model by evaluating the wrinkling occurrence using a cylindrical deep-drawing tests utilising textured tool surfaces on the blankholders. For the buckling model accuracy, the effects of different boundary condition assumption due to the tool surface constraint and yield function selection on the wrinkling occurrence were investigated. It can be concluded that the hinged boundary condition reflects the actual tool surface constraint more accurately. Moreover, using the von Mises yield criterion in the analytical buckling model exhibits better agreement with experimental results than using the Tresca yield criterion. It is also possible that the developed buckling model can be improved by introducing anisotropy yield criteria in the future.

Corresponding experiments were performed using different tool designs. The buckling model based on DMV shell theory can accurately predict the smaller texture ratio designs as well as greater draw ratios. Whilst the DMV shell theory was not suitable when the tool texture ratio was increased to a lager magnitude.

A finite element model with the implementation of dislocation-driven material model of aluminium alloy via user-defined subroutine was used to further validate the developed analytical buckling model. The onset of flange wrinkling can be computed using this FE model, and the computational results further validated the analytical buckling model for larger texture ratio cases. Differences between the analytical model predictions and FE results of the wrinkling occurrence are believed to be caused by the wrinkling onset definition in the finite element model.

Acknowledgements The research in this paper was funded by the European Union's Horizon 2020 research and innovation programme under Grant Agreement No. 723517 as part of the project "Low Cost Materials Processing Technologies for Mass Production of Lightweight Vehicles (LoCoMaTech)".

Open Access This article is distributed under the terms of the Creative Commons Attribution 4.0 International License (http://creativecommons.org/licenses/by/4.0/), which permits unrestricted use, distribution, and reproduction in any medium, provided you give appropriate credit to the original author(s) and the source, provide a link to the Creative Commons license, and indicate if changes were made.

References

1. Karbasian H, Tekkaya AE (2010) A review on hot stamping. J Mater Process Technol 210(15):2103–2118. doi:10.1016/j.jmatprotec.2010.07.019
2. Wang A, Zhong K, El Fakir O, Liu J, Sun C, Wang L-L, Lin J, Dean TA (2016) Springback analysis of AA5754 after hot stamping: experiments and FE modelling. Int J Adv Manuf Technol:1–14. doi:10.1007/s00170-016-9166-3
3. Mohamed MS, Foster AD, Lin J, Balint DS, Dean TA (2012) Investigation of deformation and failure features in hot stamping of AA6082: experimentation and modelling. Int J Mach Tools Manuf 53(1):27–38. doi:10.1016/j.ijmachtools.2011.07.005
4. Dong Y, Zheng K, Fernandez J, Li X, Dong H, Lin J (2017) Experimental investigations on hot forming of AA6082 using advanced plasma nitrocarburised and CAPVD WC: C coated tools. J Mater Process Technol 240:190–199. doi:10.1016/j.jmatprotec.2016.09.023
5. Wang M, Zhang C, Xiao H, Li B (2016) Inverse evaluation of equivalent contact heat transfer coefficient in hot stamping of boron steel. Int J Adv Manuf Technol 87(9):2925–2932. doi:10.1007/s00170-016-8678-1
6. Bruzzone AAG, Costa HL, Lonardo PM, Lucca DA (2008) Advances in engineered surfaces for functional performance. CIRP Ann Manuf Technol 57(2):750–769. doi:10.1016/j.cirp.2008.09.003
7. Costa HL, Hutchings IM (2009) Effects of die surface patterning on lubrication in strip drawing. J Mater Process Technol 209(3):1175–1180. doi:10.1016/j.jmatprotec.2008.03.026
8. Franzen V, Witulski J, Brosius A, Trompeter M, Tekkaya AE (2010) Textured surfaces for deep drawing tools by rolling. Int J Mach Tools Manuf 50(11):969–976. doi:10.1016/j.ijmachtools.2010.08.001
9. Zheng K, Politis D, Lin J, Dean T (2015) An experimental and numerical investigation of the effect of macro-textured tool surfaces in hot stamping. Int J Mater Form:1–14. doi:10.1007/s12289-015-1273-4
10. Martins J, Neto D, Alves J, Oliveira M, Menezes L (2016) Numerical modeling of the thermal contact in metal forming processes. The International Journal of Advanced Manufacturing Technology:1–15
11. Kowsarinia E, Alizadeh Y, Pour HSS (2013) Theoretical and experimental study on the effects of explosive forming parameters on plastic wrinkling of annular plates. Int J Adv Manuf Technol 67(1):877–885. doi:10.1007/s00170-012-4532-2
12. Zheng K, Politis DJ, Lin J, Dean TA (2016) A study on the buckling behaviour of aluminium alloy sheet in deep drawing with macro-textured blankholder. Int J Mech Sci 110:138–150. doi:10.1016/j.ijmecsci.2016.03.011
13. Kadkhodayan M, Moayyedian F (2011) Analytical elastic–plastic study on flange wrinkling in deep drawing process. Scientia Iranica 18(2):250–260. doi:10.1016/j.scient.2011.03.020
14. Senior BW (1956) Flange wrinkling in deep-drawing operations. Journal of the Mechanics and Physics of Solids 4(4):235–246. doi:10.1016/0022-5096(56)90032-1
15. Yu TX, Johnson W (1982) The buckling of annular plates in relation to the deep-drawing process. Int J Mech Sci 24(3):175–188. doi:10.1016/0020-7403(82)90036-4
16. Hutchinson J, Neale K (1985) Wrinkling of curved thin sheet metal. Plastic Instability:71–78
17. Niordson FI (2012) Shell theory. Elsevier Science
18. Rønning L, Hopperstad OS, Larsen PK (2010) Numerical study of the effects of constitutive models on plastic buckling of plate elements. European Journal of Mechanics - A/Solids 29(4):508–522. doi:10.1016/j.euromechsol.2010.02.001
19. Hill R (1967) The mathematical theory of plasticity. Clarendon Press
20. Wang C-T, Kinzel G, Altan T (1994) Wrinkling criterion for an anisotropic shell with compound curvatures in sheet forming. Int J Mech Sci 36(10):945–960. doi:10.1016/0020-7403(94)90056-6
21. Lin J, Mohamed M, Balint D, Dean T (2014) The development of continuum damage mechanics-based theories for predicting forming limit diagrams for hot stamping applications. International Journal of Damage Mechanics 23(5):684–701
22. Lin J, Liu Y (2003) A set of unified constitutive equations for modelling microstructure evolution in hot deformation. J Mater Process Technol 143–144:281–285. doi:10.1016/S0924-0136(03)00472-2
23. Altan T, Tekkaya AE (2012) Sheet metal forming: fundamentals. Asm International
24. Timoshenko S, Goodier JN (1951) Theory of elasticity, by S. Timoshenko and J. N. Goodier,... 2nd Edition. McGraw-Hill book Company
25. Chu E, Xu Y (2001) An elastoplastic analysis of flange wrinkling in deep drawing process. Int J Mech Sci 43(6):1421–1440. doi:10.1016/S0020-7403(00)00091-6
26. Baldwin W, Howald T (1947) Folding in the cupping operation. ASM TRANS Q 38:757–788
27. Moreira PMGP, Santos T, Tavares SMO, Richter-Trummer V, Vilaça P, de Castro PMST (2009) Mechanical and metallurgical characterization of friction stir welding joints of AA6061-T6 with AA6082-T6. Mater Des 30(1):180–187. doi:10.1016/j.matdes.2008.04.042
28. Neto D, Oliveira M, Dick R, Barros P, Alves J, Menezes L (2015) Numerical and experimental analysis of wrinkling during the cup drawing of an AA5042 aluminium alloy. International Journal of Material Forming:1–14